

# Virtual Seismometers in the Subsurface of the Earth from Seismic Interferometry

## Supplementary Material

**Andrew Curtis<sup>1,2</sup>, Heather Nicolson<sup>1,2,3</sup>, David Halliday<sup>1,2</sup>, Jeannot Trampert<sup>4</sup>,  
Brian Baptie<sup>2,3</sup>**

<sup>1</sup>*School of GeoSciences, University of Edinburgh, Grant Institute., West Mains Rd., Edinburgh EH9 3JW, UK.*

<sup>2</sup>*ECOSSE (Edinburgh Collaborative of Subsurface Science and Engineering), UK*

<sup>3</sup>*British Geological Survey, Murchison House, Kings Buildings, West Mains Road, Edinburgh, UK*

<sup>4</sup>*Faculteit Aardwetenschappen, University of Utrecht, Postbus 80.021, Utrecht, NL.*

*Correspondence to Andrew.Curtis@ed.ac.uk*

## Supplementary Methods

In this Supplementary Methods we first derive the theory of virtual receivers for acoustic and elastic media using methods similar in part to those of Wapenaar<sup>1,2</sup> and van Manen et al.<sup>3,4</sup>. It seems straightforward to extend the theory in various forms to attenuative media, to diffusive propagation, and to other wave propagation regimes<sup>5-8</sup>.

In the Supplementary Discussion below, we apply the new methods to two examples additional to those in the main text. These examples demonstrate the ability to measure both purely horizontal and purely vertical strain fields due to passing seismic waves. Measuring these fields directly has not previously been possible in seismology.

## Theory

In time-reversed acoustics, invariance of the wave equation for time-reversal can be exploited to focus a wavefield through a highly scattering medium on an original source point<sup>9</sup>. Cassereau and Fink<sup>10,11</sup> realized that the acoustic representation theorem<sup>12</sup> can be used to time-reverse a wavefield in a volume by creating secondary sources (monopole and dipole) on a surface surrounding the medium such that the boundary conditions correspond to the time-reversed components of a wavefield measured there. In an acoustic medium, the expression for the time-reversed pressure field  $P_{TR}(\mathbf{x}, t)$  at location  $\mathbf{x}$  and time  $t$  radiated from the boundary  $S$  can be written as:

$$P_{TR}(\mathbf{x}, t) = \oint_S \frac{1}{\rho} [G(\mathbf{x}, t | \mathbf{x}') * \nabla' P(\mathbf{x}', -t) - P(\mathbf{x}', -t) * \nabla' G(\mathbf{x}, t | \mathbf{x}')] \cdot \mathbf{n} \, d\mathbf{x}' \quad (1)$$

where  $G(\mathbf{x}, t | \mathbf{x}')$  denotes the Green's function of the medium,  $\nabla'G(\mathbf{x}, t | \mathbf{x}')$  denotes its gradient with respect to primed coordinates, and star denotes convolution. The medium density at the boundary and the normal to the boundary are denoted by  $\rho$  and  $\mathbf{n}$ , respectively.  $P(\mathbf{x}', -t)$  and  $\nabla'P(\mathbf{x}', -t)$  denote the time-reversal of the pressure field and its gradient. These secondary sources give rise to the back-propagating, time-reversed wavefield inside the medium that collapses onto itself at the original source location. Note that since there is no source term absorbing the converging wavefield in the original source location, it will immediately begin diverging again.

In wavefield interferometry, waves recorded at two receiver locations from a surrounding boundary of wave sources are correlated to find the Green's function between the two locations (*main text, Figure 1 - left*). Interferometry has been applied successfully to helioseismology<sup>13</sup>, ultrasonics<sup>14,15</sup>, exploration seismics<sup>16-21</sup> and seismology<sup>22-25</sup>. Recently it was shown that a link exists between the time-reversed acoustics and passive imaging disciplines, when Derode et al.<sup>26</sup> analyzed the emergence of the Green's function from field-field correlations in an open scattering medium in terms of time-reversal symmetry. As discussed in the main text, the Green's function can be recovered as long as the sources in the medium are distributed forming a perfect time-reversal device, although these geometrical constraints can often be relaxed in practice (*main text, Figure 1 - right*). A more rigorous proof for the general case was derived by Wapenaar<sup>1,27,28</sup>.

Say the initial pressure wavefield  $P(\mathbf{x}', -t)$  and  $\nabla'P(\mathbf{x}', -t)$  was that recorded on  $S$  from an impulsive source at some point  $x_l$  within the interior of  $S$ . Equation (1) reverses the entire wavefield throughout the interior of  $S$ , and hence can be used to

compute the time-reversed wavefield (including all high-order interactions) at any such location, not only the original source location. By measuring the time-reversed wavefield in a second location  $\mathbf{x}_2$ , the Green's function and its time reverse (due to the expansion of the time-reversed source field after convergence at  $\mathbf{x}_1$ ) between the source point  $\mathbf{x}_1$  and the second point  $\mathbf{x}_2$  is observed<sup>26</sup>:

$$G(\mathbf{x}_2, t | \mathbf{x}_1) - G(\mathbf{x}_2, -t | \mathbf{x}_1) = \oint_S \frac{1}{\rho} [G(\mathbf{x}_2, t | \mathbf{x}') * \nabla' G(\mathbf{x}', -t | \mathbf{x}_1) - \nabla' G(\mathbf{x}_2, t | \mathbf{x}') * G(\mathbf{x}', -t | \mathbf{x}_1)] \cdot \mathbf{n} d\mathbf{x}' \quad (2)$$

Source-receiver reciprocity gives  $G(\mathbf{x}', t | \mathbf{x}_1) = G(\mathbf{x}_1, t | \mathbf{x}')$ , so we can rewrite equation (2) so that it involves only sources on the boundary enclosing the medium:

$$G(\mathbf{x}_2, t | \mathbf{x}_1) - G(\mathbf{x}_2, -t | \mathbf{x}_1) = \oint_S \frac{1}{\rho} [G(\mathbf{x}_2, t | \mathbf{x}') * \nabla' G(\mathbf{x}_1, -t | \mathbf{x}') - \nabla' G(\mathbf{x}_2, t | \mathbf{x}') * G(\mathbf{x}_1, -t | \mathbf{x}')] \cdot \mathbf{n} d\mathbf{x}' \quad (3)$$

Thus the Green's function between two points  $\mathbf{x}_1$  and  $\mathbf{x}_2$  can be calculated once the Green's functions between the enclosing boundary and these points are known. Following the same reasoning for the acoustic case, a similar treatment for elastic waves is possible<sup>2,4</sup>. Elastic equivalents of equations (2) and (3) are found to be:

$$G_{im}(\mathbf{x}_2, -t | \mathbf{x}_1) - G_{im}(\mathbf{x}_2, t | \mathbf{x}_1) = \oint_S [G_{in}(\mathbf{x}_2, t | \mathbf{x}') * n_j c_{njkl} \partial'_k G_{lm}(\mathbf{x}', -t | \mathbf{x}_1) - n_j c_{njkl} \partial'_k G_{il}(\mathbf{x}_2, t | \mathbf{x}') * G_{nm}(\mathbf{x}', -t | \mathbf{x}_1)] d\mathbf{x}' \quad (4)$$

and

$$G_{im}(\mathbf{x}_2, -t | \mathbf{x}_1) - G_{im}(\mathbf{x}_2, t | \mathbf{x}_1) = \oint_S [G_{in}(\mathbf{x}_2, t | \mathbf{x}') * n_j c_{njkl} \partial'_k G_{ml}(\mathbf{x}_1, -t | \mathbf{x}') - n_j c_{njkl} \partial'_k G_{il}(\mathbf{x}_2, t | \mathbf{x}') * G_{mn}(\mathbf{x}_1, -t | \mathbf{x}')] d\mathbf{x}' \quad (5)$$

respectively. In the elastic case,  $c$  is the elastic stiffness tensor,  $\mathbf{n}$  is the normal vector to surface  $S$ ,  $G_{ij}(\mathbf{x}_1, t | \mathbf{x}')$  is the  $i$ th component of the particle displacement Green's tensor at location  $\mathbf{x}_1$  for a unidirectional point force in direction  $j$  at location  $\mathbf{x}'$ , and  $\partial'_k G_{ij}(\mathbf{x}_1, t | \mathbf{x}')$  is the partial derivative of the Green's tensor in the  $k$  direction with respect to primed coordinates. van Manen *et al.* used equations (3) and (5) to create a synthetic computational modelling method<sup>3,4,29</sup>. In what follows there are significant differences in methodology between acoustic and elastic cases so we address each separately.

*Acoustic case*

Equation (3) represents the Green's state with impulsive sources at locations  $\mathbf{x}'$  on the surface  $S$  recorded at locations  $\mathbf{x}_1$  and  $\mathbf{x}_2$ . Now, say instead an impulsive source was fired at location  $\mathbf{x}_2$ , and the resulting pressure signals  $\tilde{G}(\mathbf{x}', t | \mathbf{x}_2)$  and  $\nabla' \tilde{G}(\mathbf{x}', t | \mathbf{x}_2)$  were recorded at points  $\mathbf{x}'$  on  $S$  (using tilde to denote quantities derived directly from measured data in practice). By reciprocity, we would record the same signals as the case where the source occurred at  $\mathbf{x}'$  and was recorded at  $\mathbf{x}_2$ , i.e.,  $G(\mathbf{x}_2, t | \mathbf{x}') = \tilde{G}(\mathbf{x}', t | \mathbf{x}_2)$  and  $\nabla' G(\mathbf{x}_2, t | \mathbf{x}') = \nabla' \tilde{G}(\mathbf{x}', t | \mathbf{x}_2)$ . If a second source fires at location  $\mathbf{x}_1$  we obtain similarly  $G(\mathbf{x}_1, t | \mathbf{x}') = \tilde{G}(\mathbf{x}', t | \mathbf{x}_1)$  and  $\nabla' G(\mathbf{x}_1, t | \mathbf{x}') = \nabla' \tilde{G}(\mathbf{x}', t | \mathbf{x}_1)$ . Hence, by applying reciprocity to either of the acoustic equations (2) or (3) we obtain the result,

$$G^h(\mathbf{x}_2, t | \mathbf{x}_1) = \oint_S \frac{1}{\rho} \left[ \tilde{G}(\mathbf{x}', t | \mathbf{x}_2) * \nabla' \tilde{G}(\mathbf{x}', -t | \mathbf{x}_1) - \nabla' \tilde{G}(\mathbf{x}', t | \mathbf{x}_2) * \tilde{G}(\mathbf{x}', -t | \mathbf{x}_1) \right] \cdot \mathbf{n} d\mathbf{x}' \quad (6)$$

which in the frequency domain becomes (dropping angular frequency dependence from the notation),

$$G^h(\mathbf{x}_2 | \mathbf{x}_1) = \oint_S \frac{1}{\rho} \left[ \tilde{G}(\mathbf{x}' | \mathbf{x}_2) \nabla' \tilde{G}^*(\mathbf{x}' | \mathbf{x}_1) - \nabla' \tilde{G}(\mathbf{x}' | \mathbf{x}_2) \tilde{G}^*(\mathbf{x}' | \mathbf{x}_1) \right] \cdot \mathbf{n} dS'. \quad (7)$$

The left side of equations (6) and (7) is the so-called homogenous Green's function,

$G^h(\mathbf{x}_2 | \mathbf{x}_1) = G(\mathbf{x}_2 | \mathbf{x}_1) - G^*(\mathbf{x}_2 | \mathbf{x}_1)$  in the frequency domain, between the two source locations, and is obtained using Green's functions from  $\mathbf{x}_1$  and  $\mathbf{x}_2$  to the boundary location  $\mathbf{x}'$  (*main text, Figure 1 - centre*).

*Elastic case*

Equation (5) represents the Green's state in which impulsive, unidirectional, force sources at locations  $\mathbf{x}'$  on the surface  $S$  are recorded at locations  $\mathbf{x}_1$  and  $\mathbf{x}_2$ . Now, say three impulsive, unidirectional force sources in coordinate directions  $j$  were fired at location  $\mathbf{x}_2$ , and for each the three resulting particle displacement vectors in directions  $i$ ,  $\tilde{G}_{ij}(\mathbf{x}', t | \mathbf{x}_2)$  and  $\partial'_k \tilde{G}_{ij}(\mathbf{x}', t | \mathbf{x}_2)$ , were recorded at points  $\mathbf{x}'$  on  $S$ . We can obtain the Green's functions used in equation (5) by reciprocity:

$G_{ji}(\mathbf{x}_2, t | \mathbf{x}') = \tilde{G}_{ij}(\mathbf{x}', t | \mathbf{x}_2)$  and  $\partial'_k G_{ji}(\mathbf{x}_2, t | \mathbf{x}') = \partial'_k \tilde{G}_{ij}(\mathbf{x}', t | \mathbf{x}_2)$ . If a second source fires at location  $\mathbf{x}_1$  we obtain similarly  $G_{ji}(\mathbf{x}_1, t | \mathbf{x}') = \tilde{G}_{ij}(\mathbf{x}', t | \mathbf{x}_1)$  and

$\partial'_k G_{ji}(\mathbf{x}_1, t | \mathbf{x}') = \partial'_k \tilde{G}_{ij}(\mathbf{x}', t | \mathbf{x}_1)$ . Hence, by applying reciprocity to either of equations (4) or (5) we obtain the result,

$$G_{im}^h(\mathbf{x}_2, t | \mathbf{x}_1) = - \oint_S \left[ \tilde{G}_{ni}(\mathbf{x}' | \mathbf{x}_2) * n_j c_{njkl} \partial'_k \tilde{G}_{lm}(\mathbf{x}' | \mathbf{x}_1) - n_j c_{njkl} \partial'_k \tilde{G}_{li}(\mathbf{x}' | \mathbf{x}_2) * \tilde{G}_{mn}(\mathbf{x}' | \mathbf{x}_1) \right] d\mathbf{x}' \quad (8)$$

which in the frequency domain becomes (dropping angular frequency dependence from the notation),

$$G_{im}^h(\mathbf{x}_2 | \mathbf{x}_1) = - \oint_S \left[ \tilde{G}_{ni}(\mathbf{x}' | \mathbf{x}_2) n_j c_{njkl} \partial'_k \tilde{G}_{lm}(\mathbf{x}' | \mathbf{x}_1) - n_j c_{njkl} \partial'_k \tilde{G}_{li}(\mathbf{x}' | \mathbf{x}_2) \tilde{G}_{mn}(\mathbf{x}' | \mathbf{x}_1) \right] d\mathbf{x}' \quad (9)$$

The left side of equations (8) and (9) is the elastic homogenous Green's function,

$G_{im}^h(\mathbf{x}_2 | \mathbf{x}_1) = G_{im}(\mathbf{x}_2 | \mathbf{x}_1) - G_{im}^*(\mathbf{x}_2 | \mathbf{x}_1)$  in the frequency domain, between the two source locations.

### *Acoustic and Elastic case*

The right side of equations (6) and (7) [(8) and (9)] involve only time-domain cross-correlation (frequency-domain multiplications with complex conjugate) of Green's functions recorded on the surface  $S$  with sources at  $\mathbf{x}_1$  and  $\mathbf{x}_2$ . The left side, on the other hand, gives the homogenous Green's function between the two source locations. That is, these equations convert the recorded data into the data that *would have been recorded if the previous source location  $\mathbf{x}_2$  had in fact been a receiver location*. This is achieved without any approximations, and without any synthetically-modelled Green's functions. For each source point the equations require one (pressure) source in the acoustic case, and three (unidirectional force) sources in the elastic case. It also seems that derivative (dipole) sources are required, but below we will show that these can be dispensed with while still obtaining good approximations to the results.

### **Non-Impulsive Sources**

Now say the two sources at  $\mathbf{x}_1$  and  $\mathbf{x}_2$  emitted a wavefield with source signatures represented by the temporal-frequency spectra  $W_1(\omega)$  and  $W_2(\omega)$ , respectively. In the acoustic case, recordings on  $S$  would take forms similar to

$\tilde{G}(\mathbf{x}' | \mathbf{x}_i) = W_i G(\mathbf{x}' | \mathbf{x}_i)$  for  $i=1,2$ , and the cross-correlation operation in equation (7)

gives,

$$W_2 W_1^* G_h(\mathbf{x}_2 | \mathbf{x}_1) = \oint_S \frac{1}{\rho} \left[ \tilde{G}(\mathbf{x}' | \mathbf{x}_2) \nabla' \tilde{G}^*(\mathbf{x}' | \mathbf{x}_1) - \nabla' \tilde{G}(\mathbf{x}' | \mathbf{x}_2) \tilde{G}^*(\mathbf{x}' | \mathbf{x}_1) \right] \cdot \mathbf{n} d\mathbf{x}' \quad (10)$$

In the time domain then, the same cross-correlation operation gives the homogeneous Green's function convolved with the cross-correlation of the two source wavelets.

In the elastic case, if all three components of each of the two sources are excited with the same source temporal-frequency signature,  $W_1(\omega)$  and  $W_2(\omega)$  respectively for sources 1 and 2, then the cross-correlation operations in equation (9) give,

$$W_2 W_1^* G_{im}^h(\mathbf{x}_2 | \mathbf{x}_1) = - \oint_S \left[ \tilde{G}_{ni}(\mathbf{x}' | \mathbf{x}_2) n_j c_{njkl} \partial'_k \tilde{G}_{lm}(\mathbf{x}' | \mathbf{x}_1) - n_j c_{njkl} \partial'_k \tilde{G}_{li}(\mathbf{x}' | \mathbf{x}_2) \tilde{G}_{mn}(\mathbf{x}' | \mathbf{x}_1) \right] d\mathbf{x}' \quad (11)$$

Again, in the time domain, the same cross-correlation operation gives the homogeneous Green's function convolved with the cross-correlation of the two source wavelets.

### Moment Tensor Sources

We wish to apply the above theory to recordings of earthquake sources from within the earth. This requires that we create corresponding expressions from moment tensor-style sources rather than unidirectional force sources. It also requires that we develop approximations for cases where we do not have separate records for each individual component of the Green's function but instead have a set of recordings from a single source comprising a combination of different source components. In order to adapt the interferometric formulae to include moment tensors we must first apply changes that allow for the inclusion of strain sources, which correspond to single components of the moment tensor matrix. To do this we apply spatial derivatives to each of the source locations in equation (9), i.e.

$$\partial_p \partial_q G_{im}^h(\mathbf{x}_2 | \mathbf{x}_1) = - \int_S \left[ \partial_p \tilde{G}_{ni}(\mathbf{x}' | \mathbf{x}_2) n_j c_{njkl} \partial'_k \partial_q \tilde{G}_{lm}^*(\mathbf{x}' | \mathbf{x}_1) - n_j c_{njkl} \partial'_k \partial_p \tilde{G}_{li}(\mathbf{x}' | \mathbf{x}_2) \partial_q \tilde{G}_{mn}^*(\mathbf{x}' | \mathbf{x}_1) \right] d\mathbf{x}', \quad (12)$$

where  $\partial_p$  is the spatial derivative applied at  $\mathbf{x}_2$  and  $\partial_q$  is the spatial derivative applied at  $\mathbf{x}_1$ . Note that the resulting Green's function is the elastic homogeneous Green's function modulated by two independent spatial derivatives.

We can consider these strain components to represent single force couples (i.e., a pair of opposing forces defined as  $M_{ij}$ , acting in the  $i$ -direction, separated in the  $j$ -direction). If the sources at  $\mathbf{x}_1$  and  $\mathbf{x}_2$  consist of single couples then we may use equation (12) to construct spatial derivatives of the homogeneous Green's function. However, if the source consists of a combination of couples (e.g., a double-couple

Earthquake source, or an explosion) then we must make alterations to equation (12).

For such sources we define a moment tensor  $\mathbf{M}$ ,

$$\mathbf{M} = \begin{bmatrix} M_{11} & M_{12} & M_{13} \\ M_{21} & M_{22} & M_{23} \\ M_{31} & M_{32} & M_{33} \end{bmatrix}, \quad (13)$$

and from Aki and Richards<sup>30</sup> the displacement at  $\mathbf{x}_1$  due to this moment tensor source at  $\mathbf{x}_2$  is given by  $M_{pq} \partial_q \tilde{G}_{ip}(\mathbf{x}_1 | \mathbf{x}_2)$ , where Einstein's summation convention applies.

This Green's function is the  $i$ th component of displacement,  $u_i(\mathbf{x}_1 | \mathbf{x}_2)$  at  $\mathbf{x}_1$  due to a moment tensor source at  $\mathbf{x}_2$ .

For the case where we would like to obtain the Green's function between two earthquake sources we alter equation (12) by inserting moment tensors,  $\mathbf{M}^1$  and  $\mathbf{M}^2$  at the corresponding source positions  $\mathbf{x}_1$  and  $\mathbf{x}_2$ :

$$\begin{aligned} M_{ip}^2 M_{mq}^1 \partial_p \partial_q G_{im}^h(\mathbf{x}_2 | \mathbf{x}_1) = \\ \int_s \left\{ M_{ip}^2 \partial_p \tilde{G}_{ni}(\mathbf{x}' | \mathbf{x}_2) n_j c_{njkl} \partial'_k M_{mq}^1 \partial_q \tilde{G}_{lm}^*(\mathbf{x}' | \mathbf{x}_1) \right. \\ \left. - n_j c_{njkl} \partial'_k M_{ip}^2 \partial_p \tilde{G}_{li}(\mathbf{x}' | \mathbf{x}_2) M_{mq}^1 \partial_q \tilde{G}_{nm}^*(\mathbf{x}' | \mathbf{x}_1) \right\} d\mathbf{x}'. \end{aligned} \quad (14)$$

The resulting interferometric Green's functions are modulated by both of these moment tensors. The term  $n_j c_{njkl} \partial'_k M_{mq}^1 \partial_q \tilde{G}_{lm}^*(\mathbf{x}' | \mathbf{x}_1)$  is the  $n$ th component of traction,  $T_n(\mathbf{x}' | \mathbf{x}_1)$  at the boundary due to a moment tensor source. Using this

definition, and the definition of displacement above we re-write equation (14) in terms of displacement and traction,

$$M_{ip}^2 M_{mq}^1 \partial_p \partial'_q G_{im}^h(\mathbf{x}_2 | \mathbf{x}_1) = \int_s \left\{ u_n(\mathbf{x}' | \mathbf{x}_2) \cdot T_n^*(\mathbf{x}' | \mathbf{x}_1) - T_n(\mathbf{x}' | \mathbf{x}_2) \cdot u_n^*(\mathbf{x}' | \mathbf{x}_1) \right\} d\mathbf{x}' . \tag{15}$$

**Monopole Seismometers**

The right hand side of equation (14) requires both monopole (displacement,  $u_n$ ) and dipole (traction,  $T_n$ ) recordings of the energy from both moment tensor sources. Real-world seismometers only record displacement (or a time derivative thereof). In the case of particle-displacement seismometers one can usually approximate equation (14) as

210

$$M_{ip}^2 M_{mq}^1 \partial_p \partial'_q G_{im}^h(\mathbf{x}_2 | \mathbf{x}_1) = iK\omega \int_s u_n(\mathbf{x}' | \mathbf{x}_2) u_n^*(\mathbf{x}' | \mathbf{x}_1) d\mathbf{x}' \tag{16}$$

for some constant  $K$ . This is similar to approximations made in virtual source interferometry where only monopole sources are typically available (for example, Halliday and Curtis<sup>31</sup> show how such an approximation can be made for surface waves, and derive a value of  $K$  specific to that case).

If particle-velocity seismometers are used, the time-derivatives  $\dot{u}_n$  of each of the displacements  $u_n$  on the right of equation (16) are measured. The left side of equation

(16) is then obtained by taking minus (due to the complex conjugate in  $u_n^*(\mathbf{x}' | \mathbf{x}_1)$ ) a double integration in time of the right side, giving

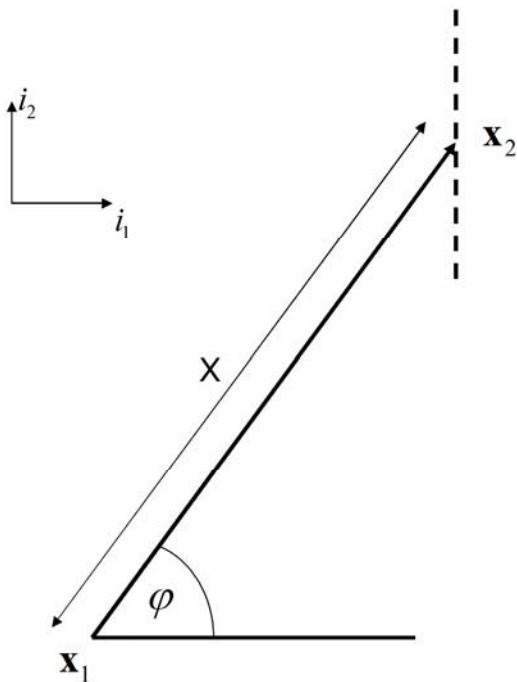
$$M_{ip}^2 M_{mq}^1 \partial_p \partial'_q \dot{G}_{im}^h(\mathbf{x}_2 | \mathbf{x}_1) = -\frac{K}{i\omega} \int_s \dot{u}_n(\mathbf{x}' | \mathbf{x}_2) \dot{u}_n^*(\mathbf{x}' | \mathbf{x}_1) d\mathbf{x}'. \quad (17)$$

Equivalently we obtain the *strain rate* on the left using,

$$M_{ip}^2 M_{mq}^1 \partial_p \partial'_q \dot{G}_{im}^h(\mathbf{x}_2 | \mathbf{x}_1) = -K \int_s \dot{u}_n(\mathbf{x}' | \mathbf{x}_2) \dot{u}_n^*(\mathbf{x}' | \mathbf{x}_1) d\mathbf{x}'. \quad (18)$$

## Surface Waves

We illustrate the above in the particular case of surface waves since to-date most applications have used that wave type. This elucidates results from real data presented in the main paper and in the Supplementary Examples.



**Supplementary Figure 1: Plan view showing geometric variables used to describe the surface wave Green's function.** The dashed line indicates the North-South fault geometry at the virtual receiver.

### Surface Wave Green's Functions

We assume that the portion of the earth in which we are interested can be approximated by a lossless, horizontally layered medium, and that in this medium the wavefield is dominated by (or can be represented by) surface waves. Further, to simplify our expressions by avoiding cross-mode inter-correlations we assume that only a single surface wave mode is present or dominant (or that modes have been separated prior to any application of interferometry<sup>31</sup>). We use a strain operator  $\mathbf{E}^\nu$  to define the spatial derivatives,

$$\mathbf{E}^\nu(\varphi) = \begin{pmatrix} ik_\nu \cos \varphi \\ ik_\nu \sin \varphi \\ \frac{\partial}{\partial z} \end{pmatrix}, \quad (19)$$

where  $k_\nu$  is the wavenumber associated with the  $\nu$ th surface wave mode and  $\varphi$  is the azimuth of the horizontal projection of the source-receiver path (*Supplementary Figure 1*). The Green's function representing a single force couple is given by applying the strain operator to equation (14) of Snieder<sup>32</sup>,

$$\partial_q G_{im}(\mathbf{x}_2 | \mathbf{x}_1) = p_i^v(z_2, \varphi) E_q^{v*} p_m^{v*}(z_1, \varphi) \frac{e^{i\left(k_v X + \frac{\pi}{4}\right)}}{\sqrt{\frac{\pi}{2} k_v X}}, \quad (20)$$

where  $z$  is positive downwards. Here  $p_i^v$  is the  $i$ th component of the polarisation vector, given for Rayleigh waves as,

$$\mathbf{p}^{vR}(z, \varphi) = \begin{pmatrix} r_1(z) \cos \varphi \\ r_1(z) \sin \varphi \\ ir_2(z) \end{pmatrix}, \quad (21)$$

and for Love waves as,

$$\mathbf{p}^{vL}(z, \varphi) = \begin{pmatrix} -l_1(z) \sin \varphi \\ l_1(z) \cos \varphi \\ 0 \end{pmatrix}, \quad (22)$$

where,  $X$  is the horizontal offset between the locations  $\mathbf{x}_1$  and  $\mathbf{x}_2$  and  $r_1^v(z)$  and  $r_2^v(z)$  are the horizontal and vertical Rayleigh wave eigenfunctions, respectively, and  $l_1^v(z)$  is the horizontal Love wave eigenvector. To simplify the expression the modal normalization  $8c^v U^v I_1^v = 1$  is assumed<sup>32</sup>, where  $c^v$ ,  $U^v$ , and  $I_1^v$  are the phase velocity, group velocity and kinetic energy for the current mode respectively. This Green's function is for a single frequency, and in the following we assume summation over the relevant frequency range. Note that when we refer specifically to Rayleigh waves or Love waves we use superscripts  $R$  and  $L$ , as in equations (21) and (22).

First we use equation (20) to define the surface wave Green's function representing the particle displacement  $\mathbf{u}(\mathbf{x}_2 | \mathbf{x}_1)$  at  $\mathbf{x}_2$  due to the general moment tensor source at  $\mathbf{x}_1$ . For Rayleigh waves this is  $\mathbf{u}^R(\mathbf{x}_2 | \mathbf{x}_1)$  with components,

$$u_1^R(\mathbf{x}_2 | \mathbf{x}_1) = M_{mq}^1 \partial_q G_{1m}^R(\mathbf{x}_2 | \mathbf{x}_1) = r_1(z_2) \cos \varphi M_{mq}^1 E_q^{v*} p_m^{v*}(z_1, \varphi) \frac{e^{i(k_v X + \frac{\pi}{4})}}{\sqrt{\frac{\pi}{2} k_v X}} \quad (23)$$

$$u_2^R(\mathbf{x}_2 | \mathbf{x}_1) = M_{mq}^1 \partial_q G_{2m}^R(\mathbf{x}_2 | \mathbf{x}_1) = r_1(z_2) \sin \varphi M_{mq}^1 E_q^{v*} p_m^{v*}(z_1, \varphi) \frac{e^{i(k_v X + \frac{\pi}{4})}}{\sqrt{\frac{\pi}{2} k_v X}} \quad (24)$$

$$u_3^R(\mathbf{x}_2 | \mathbf{x}_1) = M_{mq}^1 \partial_q G_{3m}^R(\mathbf{x}_2 | \mathbf{x}_1) = i r_2(z_2) M_{mq}^1 E_q^{v*} p_m^{v*}(z_1, \varphi) \frac{e^{i(k_v X + \frac{\pi}{4})}}{\sqrt{\frac{\pi}{2} k_v X}} \quad (25)$$

and where  $G^R$  denotes the Rayleigh wave component of the Green's function.

For Love waves the equivalent displacements  $\mathbf{u}^L(\mathbf{x}_2 | \mathbf{x}_1)$  are defined as,

$$u_1^L(\mathbf{x}_2 | \mathbf{x}_1) = M_{mq}^1 \partial_q G_{1m}^L(\mathbf{x}_2 | \mathbf{x}_1) = -l_1(z_2) \sin \varphi M_{mq}^1 E_q^{v*} p_m^{v*}(z_1, \varphi) \frac{e^{i(k_v X + \frac{\pi}{4})}}{\sqrt{\frac{\pi}{2} k_v X}}, \quad (26)$$

$$u_2^L(\mathbf{x}_2 | \mathbf{x}_1) = M_{mq}^1 \partial_q G_{2m}^L(\mathbf{x}_2 | \mathbf{x}_1) = l_1(z_2) \cos \varphi M_{mq}^1 E_q^{v*} p_m^{v*}(z_1, \varphi) \frac{e^{i(k_v X + \frac{\pi}{4})}}{\sqrt{\frac{\pi}{2} k_v X}}, \quad (27)$$

$$u_3^L(\mathbf{x}_2 | \mathbf{x}_1) = M_{mq}^1 \partial_q G_{3m}^L(\mathbf{x}_2 | \mathbf{x}_1) = 0. \quad (28)$$

where  $G^L$  denotes the Love wave component of the Green's function.

### Surface Wave Interferometry

We can now define the forward time part of the interferometric surface wave Green's function (the left side of equation (17)) as,

$$M_{ip}^2 M_{mq}^1 \partial_p \partial_q G_{im}(\mathbf{x}_2 | \mathbf{x}_1) = \left[ M_{ip}^2 E_p^v p_i^v(z_2, \varphi) \right] \left[ M_{mq}^1 E_q^{v*} p_m^{v*}(z_1, \varphi) \frac{e^{i\left(k_v X + \frac{\pi}{4}\right)}}{\sqrt{\frac{\pi}{2} k_v X}} \right]. \quad (29)$$

On the right side of this equation, the right square bracket is equal to the displacement  $\mathbf{u}$  of the appropriate surface wave. The left square bracket shows that the virtual receiver strain-response function is represented by all  $M_{ip}^2$ , the components of the moment tensor of event 2, since  $E_p^v p_i^v(z_2, \varphi)$  is simply the  $p, i$  component of strain. Hence, the virtual receiver measures the same components of strain as occurred in the original earthquake source mechanism.

Using equation (29) we can predict phase differences between interferometric estimates using different source types of moment tensor form  $\mathbf{M}^1$  and  $\mathbf{M}^2$ , since we know the form of the strain operator (equation (19)). While we may not necessarily know the different eigenvectors required to define  $\mathbf{p}^v(z_1, \varphi)$  and  $\mathbf{p}^v(z_2, \varphi)$  the above equation also shows their effect on the phase of the surface wave.

To give a feeling for what recordings at virtual sensors detect, we consider a general moment tensor source  $\mathbf{M}^1$  at location  $\mathbf{x}_1$  recorded at a virtual receiver at location  $\mathbf{x}_2$  constructed from a range of canonical example moment tensor sources. This range includes a strike-slip, a thrust, and a normal earthquake event. For a fault oriented in the North-South direction (dashed line in *Supplementary Figure 1*) we derive explicit expressions for both Love and Rayleigh waves from an event with a general moment tensor recorded at a virtual receiver with the three different source types. Although we have fixed the orientation of the fault plane to be North-South trending, we allow a general azimuth of the (horizontal projection of the) virtual receiver-to-source path. All of the following equations can therefore be applied to any fault plane geometry simply by rotating the co-ordinate axes such that the fault-plane at the virtual receiver lies in the  $i_2$  direction.

**Strike-Slip Virtual Sensor**

The scalar moment tensor for a pure left-lateral strike-slip event on a North-South trending fault (denoted  $\mathbf{M}^{SS}$ ) is then given by  $M_{12}=M_{21}=1$  with all other  $M_{ij}=0$ . Equation (29) then becomes

$$\mathbf{M}^{SS} M_{mq}^1 \partial_p \partial_q G_{im}^R(\mathbf{x}_2 | \mathbf{x}_1) = 2ik_v r_1(z_2) \cos \varphi \sin \varphi M_{mq}^1 E_q^{v*} p_m^{v*}(z_1, \varphi) \frac{e^{i\left(k_v X + \frac{\pi}{4}\right)}}{\sqrt{\frac{\pi}{2} k_v X}}, \tag{30}$$

Hence, a virtual receiver constructed from such a strike-slip event (left side of the above equation) measures the quantity on the right side, which is a scaled version of one of the horizontal components of particle displacement at location  $\mathbf{x}_2$ , i.e.

$$\mathbf{M}^{ss} M_{mq}^1 \partial_p \partial_q G_{im}^R(\mathbf{x}_2 | \mathbf{x}_1) = [2ik_v \sin \varphi] u_1^R(\mathbf{x}_2 | \mathbf{x}_1) \quad (31)$$

or

$$\mathbf{M}^{ss} M_{mq}^1 \partial_p \partial_q G_{im}^R(\mathbf{x}_2 | \mathbf{x}_1) = [2ik_v \cos \varphi] u_2^R(\mathbf{x}_2 | \mathbf{x}_1). \quad (32)$$

The terms  $ik_v \cos \varphi$  and  $ik_v \sin \varphi$  correspond to horizontal spatial derivatives (cf. equation (19)). Hence, the resulting surface waves in the preceding two equations are spatial derivatives in the  $i_2$  ( $i_1$ ) direction of the horizontal component of particle displacement in the  $i_1$  ( $i_2$ ) direction, respectively. In terms of strain, the equations represent recordings of twice the  $e_{12}$  and  $e_{21}$  components at the virtual receiver, respectively.

For Love waves we obtain

$$\mathbf{M}^{ss} M_{mq}^1 \partial_p \partial_q G_{im}^L(\mathbf{x}_2 | \mathbf{x}_1) = [ik_v \cos \varphi] u_2^L(\mathbf{x}_2 | \mathbf{x}_1) + [ik_v \sin \varphi] u_1^L(\mathbf{x}_2 | \mathbf{x}_1). \quad (33)$$

Hence, for Love waves the virtual receiver measures the sum of the horizontal derivative in the  $i_1$  direction of the particle displacement in the  $i_2$  direction, with the horizontal derivative in the  $i_2$  direction of the particle displacement in the  $i_1$  direction.

Again, this corresponds to the sum of the  $e_{12}$  and  $e_{21}$  components of strain at the virtual-receiver position.

Thus the strike-slip vertical receiver for this fault configuration is equivalent to recording various combinations of horizontal strain for both Love and Rayleigh waves.

### Thrust Virtual Sensor

The moment tensor ( $\mathbf{M}^{TF}$ ) for a thrust event on a North-South trending fault is given by  $M_{11}=-1$  and  $M_{33}=1$  with all other  $M_{ij}=0$ . For Rayleigh waves we then obtain,

$$\mathbf{M}^{TF} M_{mq}^1 \partial_p \partial_q G_{im}^R(\mathbf{x}_2 | \mathbf{x}_1) = \left( \frac{\partial}{\partial z} i r_2(z_2) - i k_v r_1(z_2) \cos^2 \varphi \right) M_{mq}^1 E_q^{\nu*} p_m^{\nu*}(z_1, \varphi) \frac{e^{i(k_v X + \frac{\pi}{4})}}{\sqrt{\frac{\pi}{2} k_v X}}, \quad (34)$$

and from equation (23) and (25) this is equivalent to

$$\mathbf{M}^{TF} M_{mq}^1 \partial_p \partial_q G_{im}^R(\mathbf{x}_2 | \mathbf{x}_1) = \frac{\partial}{\partial z} u_3^R(\mathbf{x}_2 | \mathbf{x}_1) - i k_v \cos \varphi u_1^R(\mathbf{x}_2 | \mathbf{x}_1). \quad (35)$$

So in this configuration, a virtual receiver constructed from a reverse fault measures the difference between the  $e_{33}$  and  $e_{11}$  components of strain.

For Love waves on the other hand we obtain,

$$\mathbf{M}^{TF} M_{mq}^1 \partial_p \partial_q G_{im}^L(\mathbf{x}_2 | \mathbf{x}_1) = -[ik_v(\cos \varphi)] u_1^L(\mathbf{x}_2 | \mathbf{x}_1), \quad (36)$$

or

$$\mathbf{M}^{TF} M_{mq}^1 \partial_p \partial_q G_{im}^L(\mathbf{x}_2 | \mathbf{x}_1) = [ik_v(\sin \varphi)] u_2^L(\mathbf{x}_2 | \mathbf{x}_1), \quad (37)$$

which is equivalent to recording the  $-e_{11}$  or  $e_{22}$  components of strain. This is because there is no component corresponding to  $M_{33}$  in the Love wave Green's function in a horizontally-layered, isotropic, 1-dimensional medium, and in this case  $e_{22} = -e_{11}$ .

Thus the thrust vertical receiver for this fault configuration is equivalent to recording various combinations of horizontal and vertical strains for Love and Rayleigh waves.

### Normal Virtual Sensor

The moment tensor for a normal fault is simply the negative of that for the thrust fault. Hence, by applying sign reversals to the above moment tensors we obtain the results for a normal virtual sensor.

### Exploding receiver

Finally we consider the case of a virtual receiver constructed from an explosive source. The moment tensor,  $\mathbf{M}^{\text{EX}}$ , then has  $M_{11} = M_{22} = M_{33} = 1$ , with all other  $M_{ij} = 0$ . The result is simply the sum of the diagonal components of the strain tensor  $e_{11} + e_{22} + e_{33}$ , i.e.

$$\mathbf{M}^{EX} M_{mq}^1 \partial_p \partial_q G_{im}^R(\mathbf{x}_2 | \mathbf{x}_1) = [ik_\nu \cos \varphi] u_1^R(\mathbf{x}_2 | \mathbf{x}_1) + [ik_\nu \sin \varphi] u_2^R(\mathbf{x}_2 | \mathbf{x}_1) + \frac{\partial}{\partial z} u_3^R(\mathbf{x}_2 | \mathbf{x}_1), \quad (38)$$

for Rayleigh waves and,

$$\mathbf{M}^{EX} M_{mq}^1 \partial_p \partial_q G_{im}^L(\mathbf{x}_2 | \mathbf{x}_1) = [ik_\nu \cos \varphi] u_1^L(\mathbf{x}_2 | \mathbf{x}_1) + [ik_\nu \sin \varphi] u_2^L(\mathbf{x}_2 | \mathbf{x}_1), \quad (39)$$

for Love waves (since again there is no component corresponding to  $M_{33}$  in this Love wave Green's function).

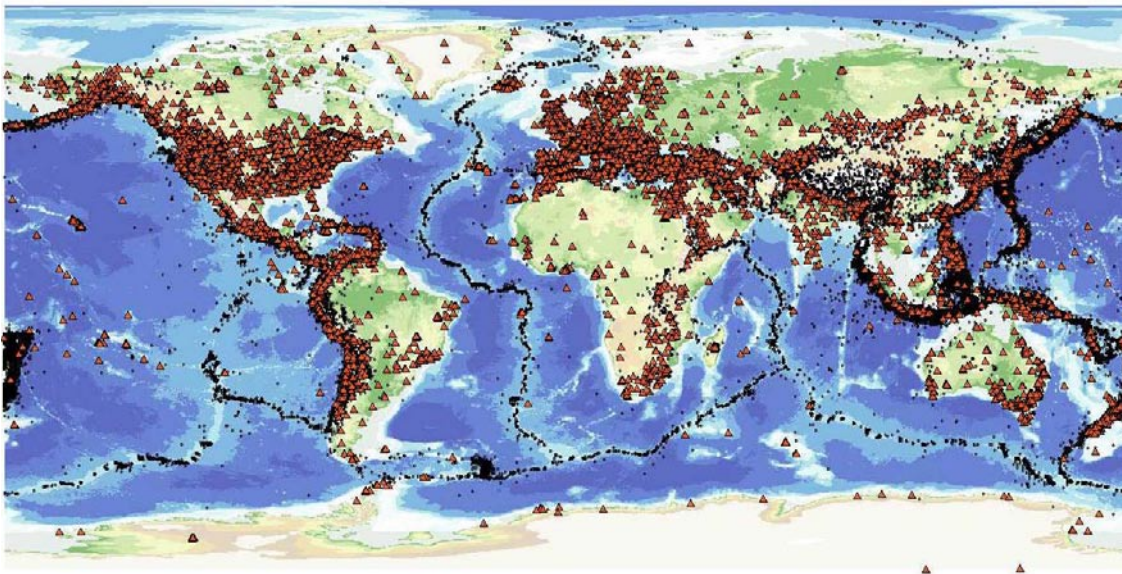
### Moment Tensor Summary

The above examples illustrate how we can use theoretical Green's functions to investigate the effect of cross-correlating recordings from two sources that can be represented by moment tensors. We find that, by using moment tensor sources at virtual-receiver locations the resulting surface wave estimates can be considered to be combinations of spatial derivatives of particle displacement (i.e. strain sensors). Moment tensors are readily available for most sizeable earthquakes, hence similar analysis to the above can be used to understand the different Green's functions estimated using virtual receiver seismic interferometry for real earthquakes. This may be important as in conventional earthquake seismology, data contains a receiver response function and a moment tensor source function. However, in virtual receiver interferometry the moment tensor at the virtual receiver location becomes a moment

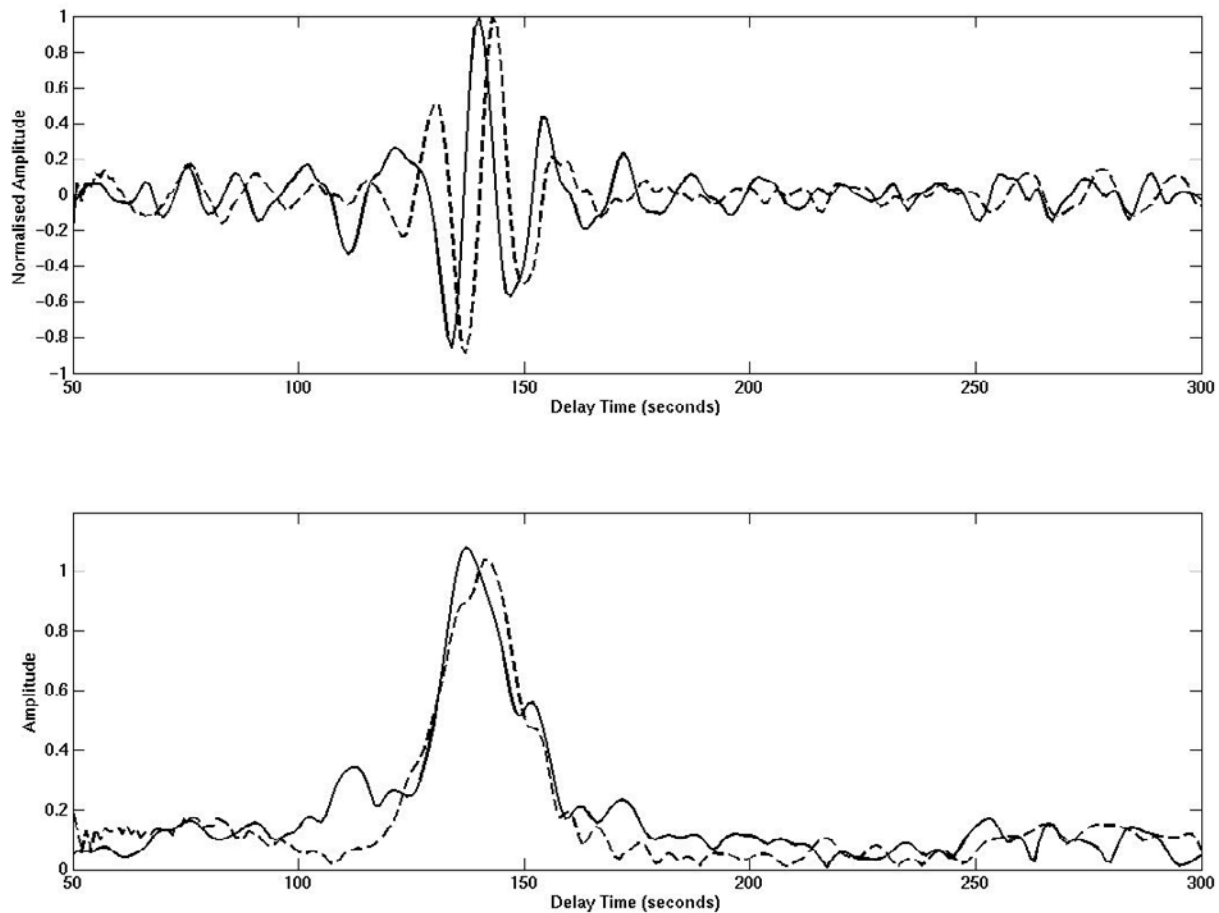
tensor sensor. Conventional approaches to data analysis may therefore require some development in order to use this new data type.

## Supplementary Discussion

*Supplementary Figure 2* shows that the distribution of sources and receivers of seismic energy are spatially strongly biased. Consequently most of the Earth's subsurface can only be interrogated using long earthquake-to-receiver, or receiver-to-receiver paths of energy propagation. The methods presented here allow source-to-source paths to be used, potentially spanning some of the previously poorly sampled regions of the Earth with relatively short paths.



**Supplementary Figure 2. Global distribution of earthquakes of magnitude > 5 since 1973 (circles) and 13,000 NEIC-listed seismometers (triangles).**

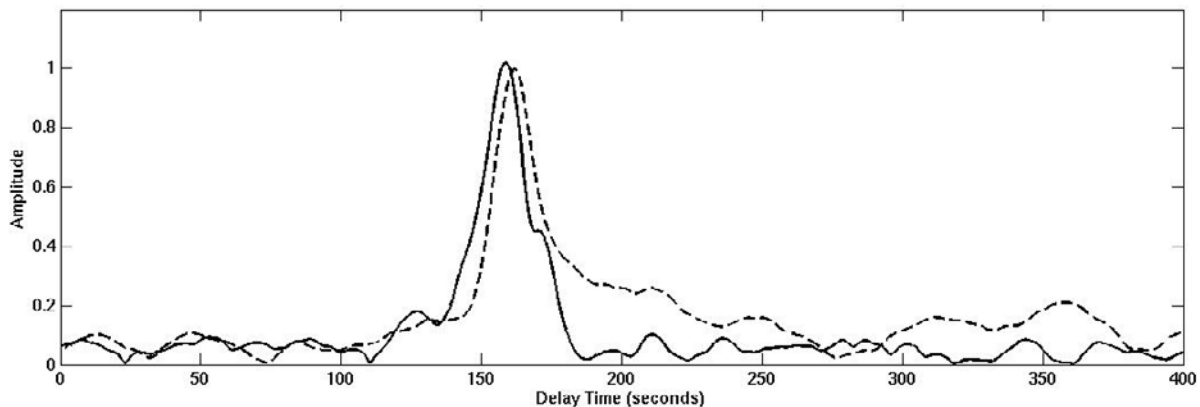
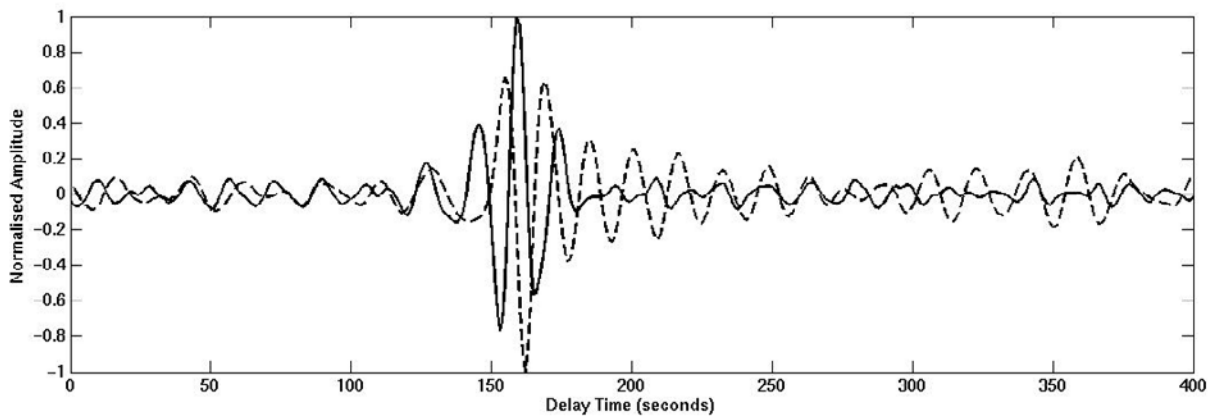


**Supplementary Figure 3. Comparison of Real and Virtual Seismograms.** Comparison of recordings of earthquake 1 by the strike-slip virtual receiver 3 and the real seismometer MLAC: seismograms (top) and envelope functions (bottom) recorded at the virtual receiver (solid line) and the inverted time-derivative of the radial-component seismogram from MLAC (dashed). Signals are constructed by cross-correlation and stacking of 20 stations from the USArray and Berkeley seismic networks (Figure 3 in main text). Amplitudes are normalised and all traces are band-passed between 15 and 33 seconds.

A virtual sensor constructed from the strike-slip earthquake 3 oriented at 45 degrees to the East-West energy propagation path (Figure 3, main text) measures the sum of  $e_{12}$  and  $e_{21}$  components of strain (**Supplementary Table 1**). A comparable scaled strain measurement can be calculated from the neighbouring seismometer by

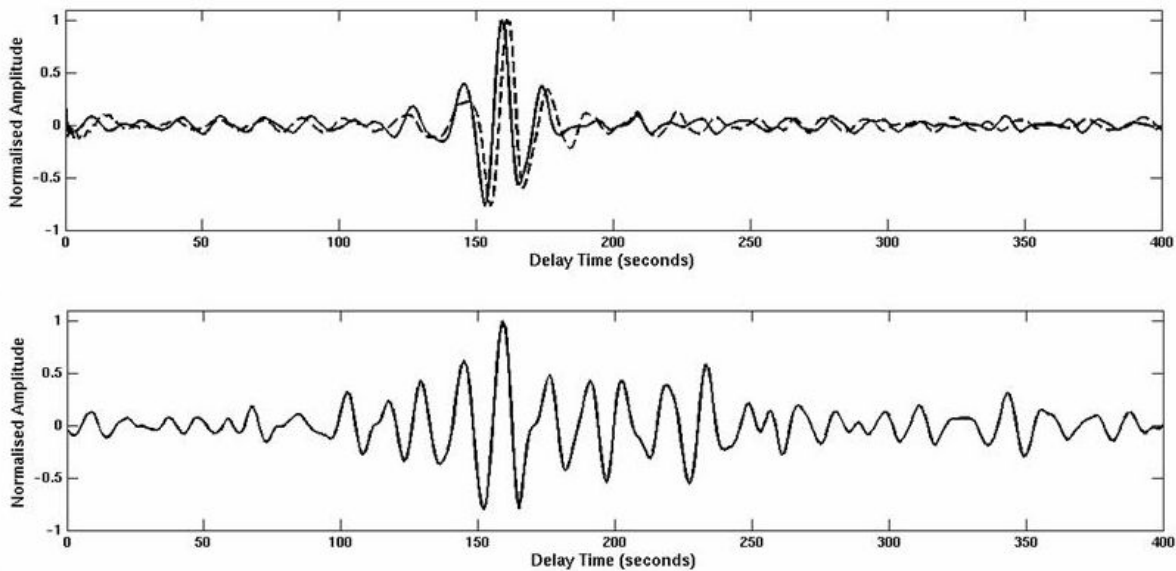
taking the (negative of the) time-derivative of the radial component of velocity.

**Supplementary Figure 3** shows a comparison between this time derivative and the virtual receiver record. The group arrival of the main energy matches to within 5s, as does the phase. A phase mismatch of 5s is easily accounted for by the difference between temporal responses of virtual and real seismometers as described in the Methods section.



**Supplementary Figure 4. Comparison of Real Vertical Component, and Virtual Vertical Strain Seismograms.** Similar to Supplementary Figure 3, but here using the normal virtual receiver 4 (solid), and the direct recording is the inverted, vertical-component seismogram from seismometer R06C (dashed). Virtual receiver records are constructed using 15 stations from the USArray and Berkeley seismic networks (Figure 3 in main text).

**Supplementary Figure 4** shows the same event recorded by the virtual sensor constructed from the N-S oriented normal-faulting earthquake 4. This virtual receiver measures the difference between the  $e_{33}$  and  $e_{11}$  components of strain. There is no easy way to construct a comparison measurement for the  $e_{33}$  component from the real seismometer so in Supplementary Figure 4 the comparison seismogram is simply the vertical component of particle velocity. As expected, while the energy group arrival times are again well matched, the phases differ markedly.



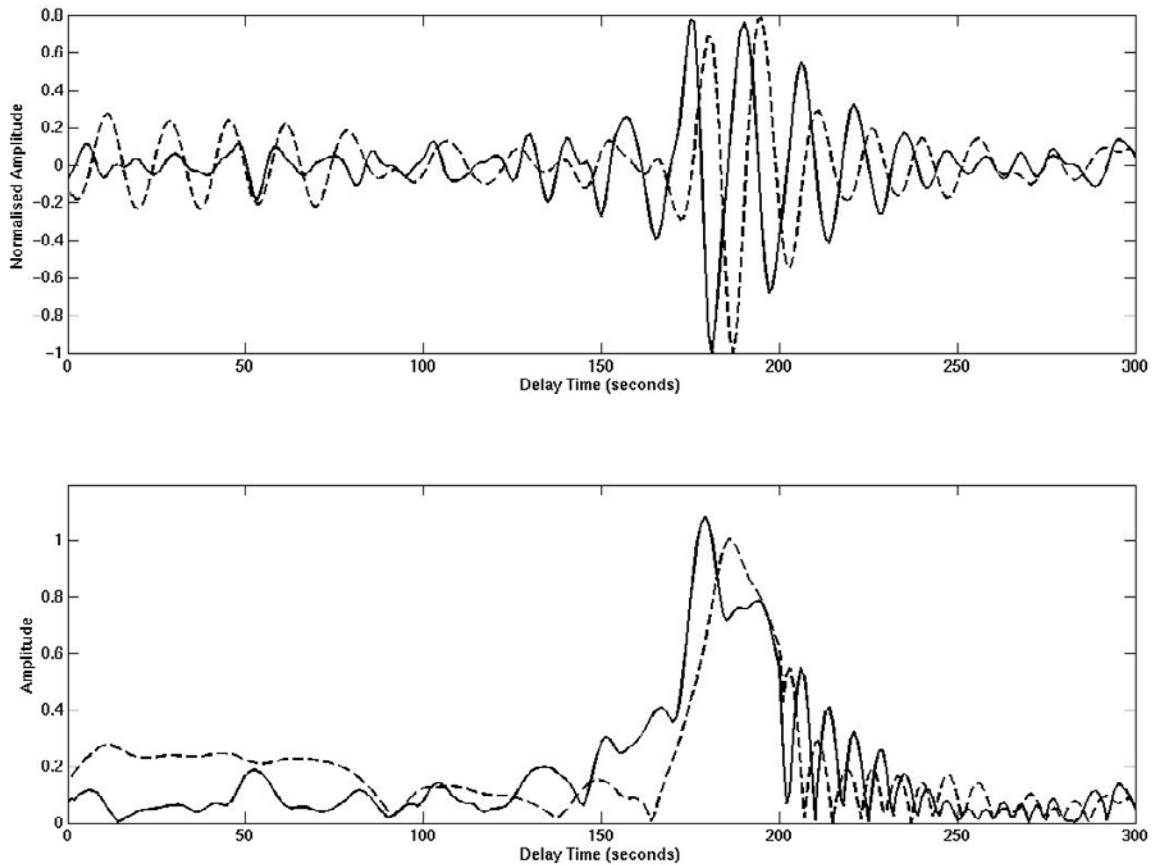
**Supplementary Figure 5. Comparison of Current Method with that of Hong and Menke.**

Top: comparison of seismograms of earthquake 1 recorded by the normal virtual receiver 4 (solid) with the directly-recorded, inverted, time derivative of the radial-component measurements from seismometer R06C (dashed), as in Figure 4 of the main text. Lower panel is the equivalent result obtained using the method of Hong and Menke (2006).

In Figure 4 of the main text and in the top plot of *Supplementary Figure 5* we show that the recording from the virtual sensor constructed from the N-S oriented, normal-fault earthquake 4 compares remarkably well with the measurement of the  $e_{11}$  component of strain (estimated from the time derivative of the horizontal seismogram from the neighbouring sensor). Previously, Hong and Menke<sup>33</sup> estimated virtual seismograms by constructing pseudo-noise sequences from earthquake coda waves. In the lower plot of *Supplementary Figure 5* we show that their method produces relatively inaccurate seismogram approximations for reasons explained in the main text.

Vertical strains are fundamentally new measurements provided by the virtual sensors. We can isolate the vertical derivative measurement by looking at seismograms from earthquakes occurring along-strike of the normal virtual sensor. In this geometry the  $e_{11}$  component is zero, leaving only the  $e_{33}$  component (equation (35) – SM).

**Supplementary Figure 6** shows the vertical strain seismogram recorded on the normal virtual receiver from the southernmost earthquake in Figure 3 of the main text. Again, the energy group arrival time is reasonable given that observed on the vertical particle velocity record, while the phase of the vertical strain is an example of a new type of measurement to seismology.



**Supplementary Figure 6. Comparison of Real and Virtual Vertical Strain Seismograms.**

Similar to Supplementary Figure 3, but compares recordings of earthquake 2 at the normal virtual receiver and the real seismometer R06C: the inverted, vertical component seismogram is shown (dashed). Signals are constructed by cross-correlation and stacking of 14 stations from the USArray and Berkeley seismic networks (Figure 3 in main text).

<b>Thrust Fault Earthquake</b>	$e_{33} - e_{11}$
<b>Normal Earthquake</b>	$e_{11} - e_{33}$
<b>Strike-Slip Earthquake</b>	$e_{12} + e_{21}$
<b>Isotropic Explosion</b>	$e_{11} + e_{22} + e_{33}$

**Supplementary Table 1: Combinations of strain components  $e_{ij}$  measured for each canonical source mechanism.** We use a left-handed coordinate system with axes 1, 2 and 3 pointing East, North and down, respectively. The earthquake fault plane is assumed to be oriented (strike) Northwards, the strike-slip fault plane is vertical while the thrust and normal fault planes have 45 degrees dip. No fault is assumed for the explosion.

## References

- <sup>1</sup> Wapenaar, K., Retrieving the elastodynamic Green's function of an arbitrary inhomogeneous medium by cross correlation. *Phys. Rev. Lett.* **93**, 254301-254301 - 254301-254304 (2004).
- <sup>2</sup> Wapenaar, K. & Fokkema, J., Green's function representations for seismic interferometry. *Geophysics* **71**, SI33-SI44 (2006).
- <sup>3</sup> van Manen, D.-J., Robertsson, J.O.A., & Curtis, A., Modeling of wave propagation in inhomogeneous media. *Phys. Rev. Lett.* **94**, pp. 164301-164301 - 164301-164304 (2005).
- <sup>4</sup> van Manen, D.-J., Curtis, A., & Robertsson, J.O.A., Interferometric modeling of wave propagation in inhomogeneous elastic media using time reversal and reciprocity. *Geophysics* **71** (No. 4), SI47-SI60 (2006).
- <sup>5</sup> Slob, E., Draganov, D., & Wapenaar, K., Interferometric electromagnetic Green's functions representations using propagation invariants. *Geophys. J. Int.* **169**, 60-80 (2007).
- <sup>6</sup> Slob, E. & Wapenaar, K., Electromagnetic Green's functions retrieval by cross-correlation and cross-convolution in media with losses. *Geophysical Research Letters* **34**, L05307-05301 - L05307-05305 (2007).
- <sup>7</sup> Snieder, R., Extracting the Green's function of attenuating heterogeneous media from uncorrelated waves. *J. Acoust. Soc. Am.* **121**, 2637-2643 (2007).

- 8 Snieder, R., Wapenaar, K., & Wegler, U., Unified Green's function retrieval  
by cross-correlation; connection with energy principles. *Phys. Rev. E* **75**,  
036103 (2007).
- 9 Derode, A., Roux, P., & Fink, M., Robust Acoustic Time Reversal with High-  
Order Multiple Scattering. *Phys. Rev. Lett.* **75**, 4206-4209 (1995).
- 10 Cassereau, D. & Fink, M., Time-Reversal of Ultrasonic Fields - Part III:  
Theory of the Closed Time-Reversal Cavity. *IEEE Trans. Ultrason.*  
*Ferroelectr. Freq. Control* **39** (5), 579-592 (1992).
- 11 Cassereau, D. & Fink, M., Focusing with Plane Time-Reversal Mirrors: an  
Efficient Alternative to Closed Cavities. *J. Acoust. Soc. Am.* **94**, 2373 (1993).
- 12 Wapenaar, K. & Fokkema, J., Reciprocity Theorems for Diffusion, Flow, and  
Waves. *J. Appl. Mech.* **71** (1), 145-150 (2004).
- 13 Rickett, J.E. & Claerbout, J.F., Calculation of the sun's acoustic impulse  
response by multi-dimensional spectral factorization. *Sol. Phys.* **192** (203-210)  
(2000).
- 14 Lobkis, O.I. & Weaver, R.L., Ultrasonics without a Source: Thermal  
Fluctuation Correlations at MHz Frequencies. *Phys. Rev. Lett.* **87** (no. 13)  
(2001).
- 15 Weaver, R.L. & Lobkis, O.I., On the emergence of the Green's function in the  
correlations of a diffuse field. *J. Acoust. Soc. Am.* **110** (no. 6), pp. 3011-3017  
(2001).
- 16 Bakulin, A. & Calvert, R., Virtual Source: new method for imaging and 4D  
below complex overburden. *74th Annual International Meeting, SEG,*  
*Expanded Abstracts*, 2477-2480 (2004).

- 17 Draganov, D., Wapenaar, K., & Thorbecke, J., Passive seismic imaging in the presence of white noise sources. *The Leading Edge* **23** (9), 889-892 (2004).
- 18 Bakulin, A. & Calvert, R., The virtual source method: Theory and case study. *Geophysics* **71**, SI139-SI150 (2006).
- 19 Mehta, K., Bakulin, A., Sheiman, J., Calvert, R., & Snieder, R., Improving the virtual source method by wavefield separation. *Geophysics* **72** (No. 4), pp. V79–V86 (2007).
- 20 Vasconcelos, I.R., Snieder, R., & Hornby, B., Target-oriented interferometry - Imaging with internal multiples from subsalt VSP data. *77th Annual International Meeting, SEG, Expanded Abstracts*, 3069-3073 (2007).
- 21 Halliday, D.F., Curtis, A., & Kragh, E., Seismic surface waves in a suburban environment – active and passive interferometric methods. *The Leading Edge* **27** (no. 2), 210-218 (2008).
- 22 Campillo, M. & Paul, A., Long-Range Correlations in the Diffuse Seismic Coda. *Science* **299** (5606), 547 - 549 (2003).
- 23 Shapiro, N. & Campillo, M., Emergence of broadband Rayleigh waves from correlations of the ambient seismic noise. *Geophysical Research Letters* **31**, L07614 (2004).
- 24 Snieder, R., Extracting the Green's function from the correlation of coda waves: A derivation based on stationary phase. *Phys. Rev. E* **69**, 046610 (2004).
- 25 Shapiro, N., Campillo, M., Stehly, L., & Ritzwoller, M., High-Resolution Surface-Wave Tomography from Ambient Seismic Noise. *Science* **307**, 1615-1617 (2005).

- <sup>26</sup> Derode, A. *et al.*, Recovering the Green's function from field-field correlations in an open scattering medium. *J. Acoust. Soc. Am.* **113** (6), 2973-2976 (2003).
- <sup>27</sup> Wapenaar, K., Synthesis of an inhomogeneous medium from its acoustic transmission response. *Geophysics* **68** (no. 5) (2003).
- <sup>28</sup> Wapenaar, K., Thorbecke, J., & Draganov, D., Relations between reflection and transmission responses of three-dimensional inhomogeneous media. *Geophys. J. Int.* **156**, 179-194 (2004).
- <sup>29</sup> van Manen, D.-J., Robertsson, J.O.A., & Curtis, A., Exact wavefield simulation for finite-volume scattering problems. *J. Acoustic. Soc. Am. Express Letters* **122** (No. 4), pp. EL115-EL121 (2007).
- <sup>30</sup> Aki, K. & Richards, P.G., Quantitative Seismology. *University Science Books, California* (2002).
- <sup>31</sup> Halliday, D.F. & Curtis, A., Seismic interferometry, surface waves, and source distribution. *Geophys. J. Int.* **175** (no. 3), 1067-1087 (2008).
- <sup>32</sup> Snieder, R., Scattering of surface waves. , in *Scattering and Inverse Scattering in Pure and Applied Science*, Eds. Pike, R. and P. Sabatier, Academic Press, San Diego, 562-577 (2002).
- <sup>33</sup> Hong, T.-K. & Menke, W., Tomographic investigation of the wear along the San Jacinto fault, southern California. *Phys. Earths Planet. Inter.* **155** (3-4), 236-248 (2006).